Supporting Information

True Vapor–Liquid–Solid Process Suppresses Unintentional Carrier Doping of Single Crystalline Metal Oxide Nanowires

Hiroshi Anzai[1], Masaru Suzuki[1], Kazuki Nagashima[1], Masaki Kanai[1], Zetao Zhu[1], Yong He[1], Mickaël Boudot[1], Guozhu Zhang[1], Tsunaki Takahashi[1], Katsuichi Kanemoto[2], Takehito Seki[3], Naoya Shibata[3] and Takeshi Yanagida[1*]

[1] Institute for Materials Chemistry and Engineering, Kyushu University, 6-1 Kasuga-Koen, Kasuga, Fukuoka 816-8580, Japan

[2] Department of Physics, Osaka City University, 3-3-138 Sugimoto, Sumiyoshi-ku, Osaka 558-8585, Japan

[3] Institute of Engineering Innovation, University of Tokyo, 2-11-16 Yayoi, Bunkyo-ku, Tokyo 113-8656, Japan

*yanagida@cm.kyushu-u.ac.jp

S1. Models for electrical conductivity of tapered SnO_2 nanowires.

As shown in Figure S1, we consider the three models to understand the electrical properties of tapered SnO_2 nanowire, including 1) “homogeneous conduction model”, 2) “surface depletion model”, and 3) “VS-LS model”. In the former two models (homogeneous model and surface depletion model), the electrical resistance is inversely proportional to the cross-sectional area. Note that in the surface depletion model, the observed nanowire resistance might be higher than that for the homogeneous model due to the presence of depletion layer at the contact between electrode and nanowire. The experimental data in Figure 2c of main manuscript highlighted that the resistance change cannot be explained by either the homogeneous model or the surface depletion model, since the resistance value changed almost 3 orders when the nanowire diameter ranged from 58 nm to 135 nm. This indicates that the electrical conduction in SnO_2 nanowires is spatially inhomogeneous. Thus, it seems that the VS-LS model seems to be more appropriate to explain the spatial conductivity of tapered nanowires in terms of the conductive outer VS crystal and the insulative inner LS crystal.

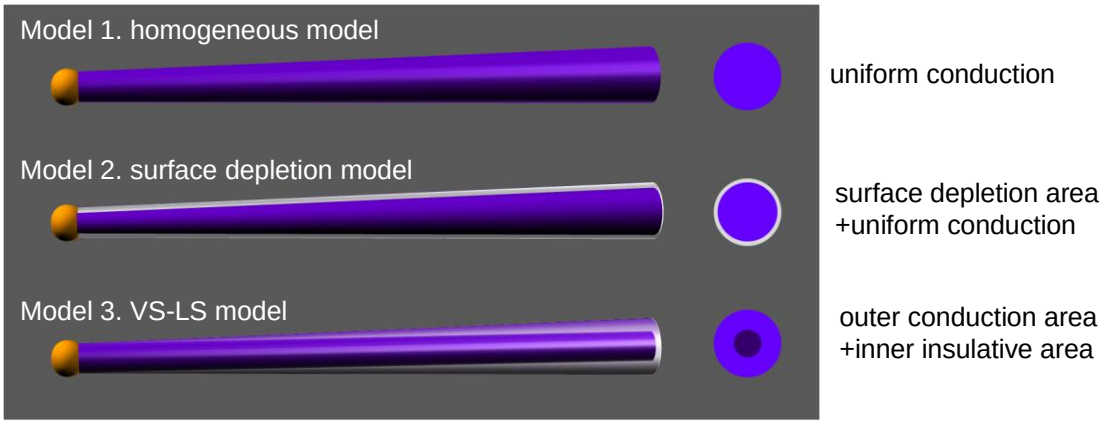

Figure S1 Models of electrical conductivity of tapered SnO_2 nanowire.

S2. Spatial distribution analysis of electrical conductivity of tapered SnO_2 nanowire when varying the oxygen partial pressure during crystal growth.

Here, we show the spatial distribution analysis of electrical conductivity within a tapered SnO_2 nanowire when varying the oxygen partial pressure. Since metal oxide nanowires are composed of metal and oxygen elements, the sidewall crystal growth can be introduced by oxygen flux variation. Figure S2 (a) shows oxygen flux (oxygen partial pressure: P_{O2}) dependence on the diameter of SnO_2 nanowires. These SnO_2 nanowires were grown under the conditions, including the Sn flux (8.0×10^{17} cm^2s^{-1}), the growth temperature (750^{o}C) and Au catalysts (~1nm). It should be noted that the SnO_2 nanowires growth was not observable at this Sn flux range when P_{O2} was lower than 10^{-4} Pa. While the nanowire growth occurred at P_{O2} >10^{-4} Pa, the sidewall growth was not seen at P_{O2} <10^{-3} Pa. This is consistent with the results in Figure 1f of main manuscript, in which the sidewall area starts to grow with Sn flux over 15×10^{17} $cm^{-2}s^{-1}$ and P_{O2} of 10^{-3} Pa. The clear sidewall growth was seen when P_{O2} >10^{-2} Pa. Figure S2 (b) shows the FESEM image of single SnO_2 nanowire device bridged by multi-nanoelectrodes. The SnO_2 nanowire was grown at P_{O2} 10^{-2} Pa. The gap size was 430 nm. Figure S2 (c) shows the measured spatial distribution data of 4-probe resistances in tapered SnO_2 nanowire. The resistances changed by 3 orders when the nanowire diameter changed from 37 nm to 51 nm. As a comparison, the calculated resistance values by assuming the homogeneous electrical conduction are also shown in the figure. (The data was calibrated with resistance value at 37 nm) The comparison clearly highlights that the electrical conduction in SnO_2 nanowire cannot be explained by the homogeneous conduction model, and the VS crystal

is more conductive than LS crystal even when the VS crystal is created by oxygen flux. Thus these results highlight that the electrical conduction observed in tapered SnO_2 nanowire was not due to the excess Sn flux supply, and the VS and LS interfaces play crucial role on the unintentional doping event during crystal growth.

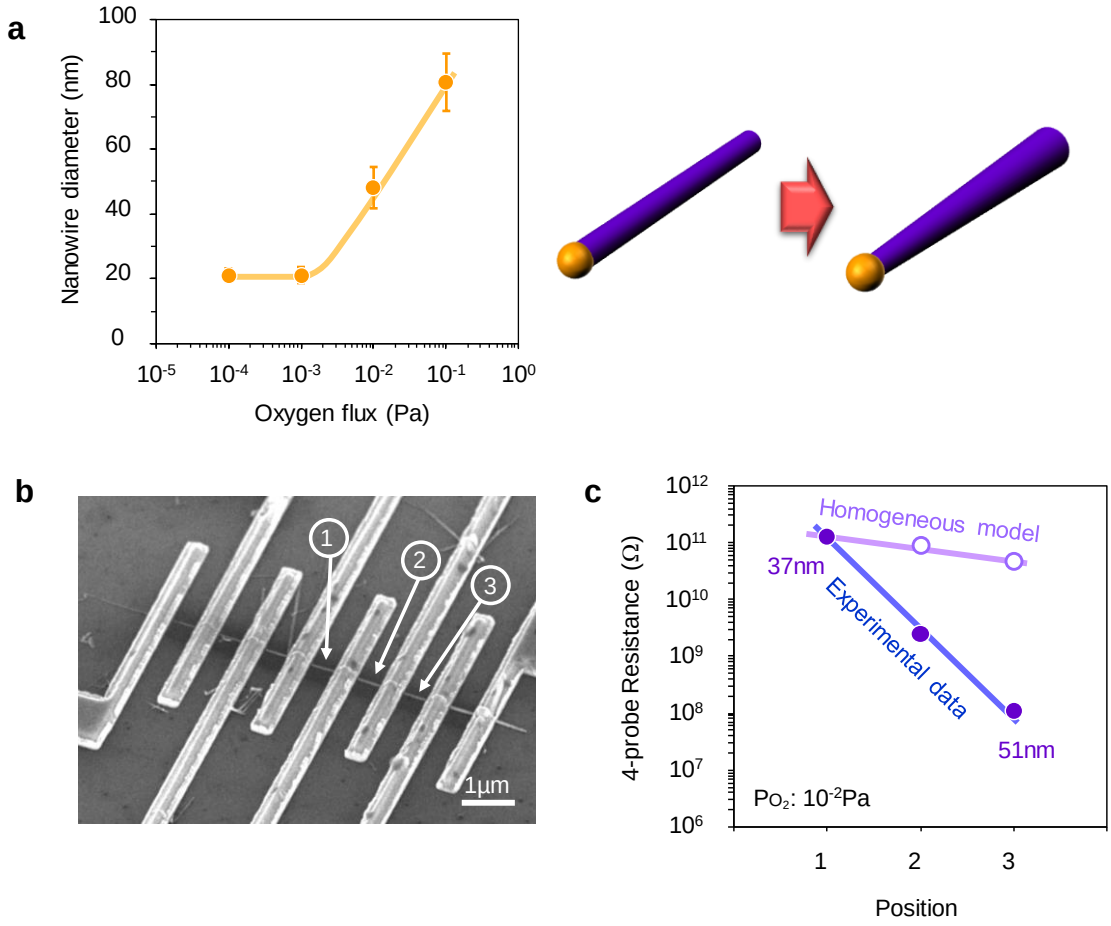

Figure S2 a) Morphology variation of tapered SnO_2 nanowire when varying the oxygen partial pressure during growth, b) SEM image of fabricated multi-probe device to measure the spatial distribution of electrical resistivity of tapered SnO_2 nanowire, and c) Spatial distribution data of 4-probe resistance with comparison to homogeneous electrical conduction model.

S3. XRD analysis of tapered and untapered SnO_2 nanowires.

We performed x-ray diffraction (XRD) analysis (Cu Kα, λ=1.5418 Å) to evaluate the crystallinity of tapered and untapered SnO_2 nanowires, Figure S3 shows XRD patterns of tapered SnO_2 nanowires (purple line, Sn flux: 27.2×10^{17} $cm^{-2}s^{-1}$) and untapered SnO_2 nanowires (red line, Sn flux: 10.4×10^{17} $cm^{-2}s^{-1}$). Only SnO_2 {101} peaks were observed for both samples in the scan range of 20-90°, indicating the single crystalline nature of both fabricated SnO_2 nanowires. However, there are no significant difference between the two nanowires on the XRD data since the XRD data is spatially averaged.

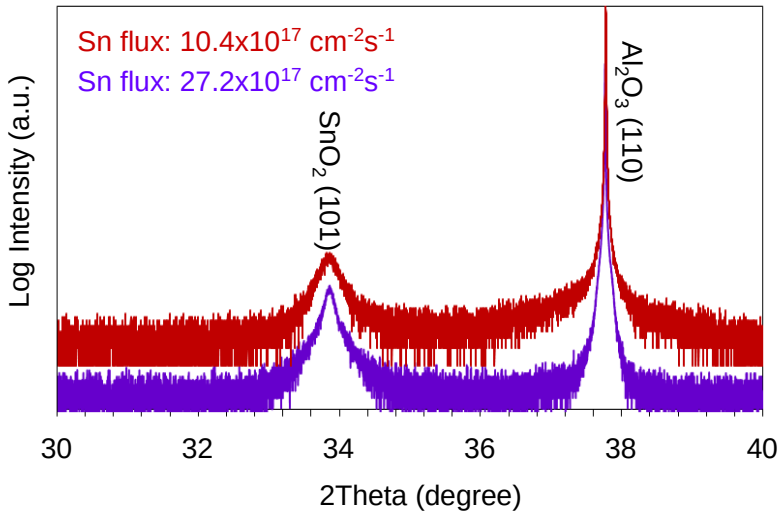

Figure S3. XRD data of tapered and untapered SnO_2 nanowires.

S4. Ultraviolet-visible (UV-vis) absorption analysis of tapered and untapered SnO_2 nanowires.

We performed an ultraviolet-visible (UV-vis) absorption spectroscopy measurement for tapered and untapered SnO_2 nanowires. The wavelength range of this measurement was 190-900 nm. The absorption spectra of the SnO_2 nanowires were obtained by subtracting the background signals from a both side polished Al_2O_3 (110) substrate. Figure S4 shows field-emission scanning electron microscopy (FESEM) images of untapered (Sn flux: 8.73×10^{17} $cm^{-2}S^{-1}$) and tapered (Sn flux: 52.3×10^{17} $cm^{-2}s^{-1}$) SnO_2 nanowires grown onto both side polished Al_2O_3 (110) substrates. Figure S4 also shows the absorption spectra as a function of incident light energy. These spectra were normalized by adjusting at the maximum intensity. The results showed that tapered SnO_2 nanowires have the stronger absorption at the energy less than 3 eV compared with untapered SnO_2 nanowires. This indicates that more energy states exist within the band gap (3.6 eV) for the tapered SnO_2 nanowires.

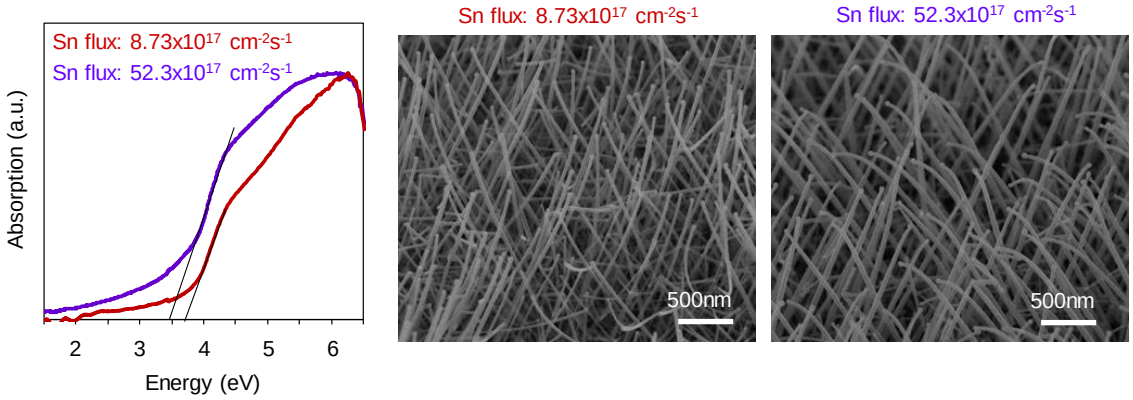

Figure S4. UV-vis absorption spectroscopy data of tapered and untapered SnO_2 nanowires.

S5. Principal component analysis (PCA) of EELS spectra for cross-sectional SnO_2 nanowires

In order to reveal a spatial distribution of the spectrum deviation, the EELS spectra were obtained from two dimensional regions (9×11 pixels for the VS-rich nanowire and 7×9 pixels for the VS-less nanowire). The VS-rich and the VS-less SnO_2 nanowire were fabricated with Sn flux 47.3×10^{17} cm^2s^{-1} and 12.3×10^{17} cm^2s^{-1}. Data acquisition time for each pixel is 5 sec. During the acquisitions, the probe scanned inside each pixel. The pixel sizes for VS-rich and VS-less nanowire are 4.3 nm and 2.0 nm, respectively. After the energy-drift correction, principal component analysis was performed for the 99 and the 63 spectra dataset, respectively. Figure S5 shows the principal component analysis (PCA) for the cross-sectional (a) VS-rich and (b) VS-less SnO_2 nanowire. The figure contains the data including the extracted EELS components (Component 1 and Component 2), the HAADF image and the amplitude maps created by Component 1 and Component 2. For VS-rich nanowire (figure S5 (a)), the Component 2 contains two significant peaks corresponding to O-K edge, in which intensity ratio of the 2nd peak to the 1st one is higher than Component 1. Spectra with high and low intensity ratio indicate stoichiometric SnO_2 and nonstoichiometric $SnO_{2-\delta}$ (Figure 3c), respectively. Therefore, the darker pixels located at surface area in the amplitude map for Component 2 of VS-rich nanowire indicate the inhomogeneous stoichiometry of SnO_2 and the presence of unintentional doping at the surface area. On the other hand, for VS-less nanowire (figure S5 (b)), intensities of two small peaks corresponding to O-K edge in Component 2 are comparable to random noise around the peaks and the

homogeneous stoichiometric distribution was seen in the amplitude map. It indicates the spectra data of VS-less nanowire exhibit no spatial dependence. Combined with the result of spatially resolved EELS spectra shown in figure 3, we conclude that the unintentional doping is drastically suppressed in the VS-less SnO_2 nanowire.

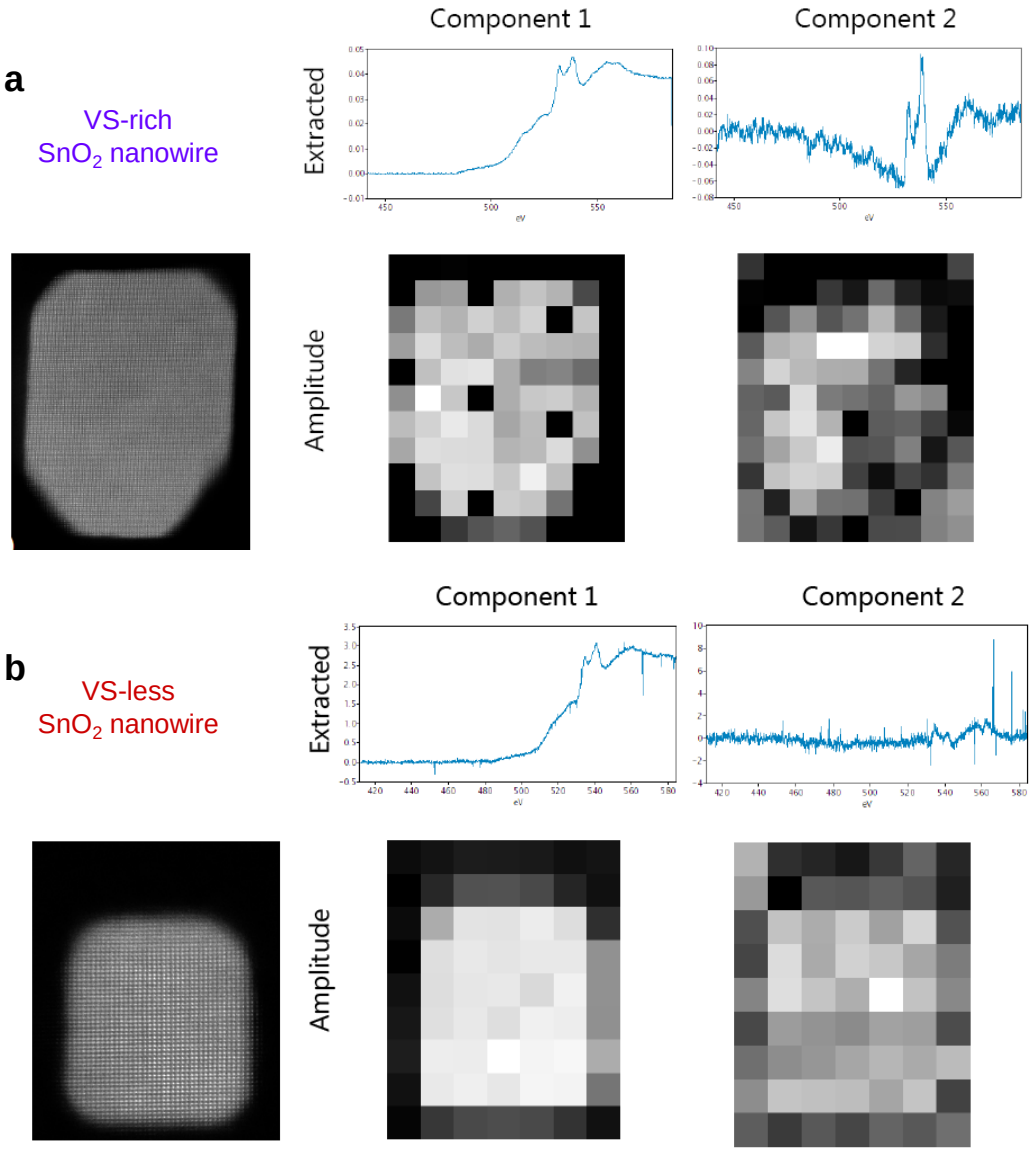

Figure S5 Principal component analysis (PCA) of EELS spectra for cross-sectional SnO_2 nanowires. Figure S5a shows the data of VS-rich SnO2 nanowire, ad Figure S5b shows the data of VS-less SnO2 nanowire.

S6. Calculation details of MD simulations

The molecular dynamics (MD) simulation can express time-evolution of motion (position and translation speed) for each of particles which interact with each other through short-range Lenard-Jones (*L-J*) interaction. In this simulation system, four types of particles (A, B, A' and C) were utilized to model vapor-liquid-solid (VLS) growth process. Here, A and C can make AC compound in solid phase which expresses an oxide formation, A' is an impurity atom, and B is assigned as solvent liquid atom. Following *L-J* type potential is used as 2-body interaction potential except the interaction between A-A and C-C.

$$\emptyset(r_{ij}) = 4\varepsilon\left[\left(\frac{\sigma_{ij}}{r_{ij}}\right)^{12} - \left(\frac{\sigma_{ij}}{r_{ij}}\right)^{6}\right] + \emptyset_{corr}(r_{ij}) \quad (1)$$

Here, r_{ij} means distance between the interacted two particles (center-to-center distance), σ_{ij} is sum of the respective particles radii and ε expresses the bonding energy constant defined for respective particle combination, ε_{BB}, ε_{AB}, ε_{CB} and ε_{AC} independently. A' particle is identical with A particle, except for the bonding energy with C particle, $\varepsilon_{A'C}(\equiv \varepsilon'\varepsilon_{AC})$. To accelerate the calculation speed, long range interaction is neglected in this program code with inducing cut-off distance, Rc (set to be Rc=3σ_{ij}), and $\phi(r_{ij})$ is set to be zero with r_{ij}>R_c. The correction term ϕ_{corr} is set to satisfy the continuity of ϕ and $\mathrm{d}\phi/\mathrm{d}r$ at r_{ij}=R_c.

For the potential between A-A and C-C, other modified *L-J* potential is used.

$$\emptyset(r_{ij}) = 4\varepsilon\left[\left(\frac{\sigma_{ij}}{r_{ij-l_0}}\right)^{12} - \left(\frac{\sigma_{ij}}{r_{ij-l_0}}\right)^{6}\right] + \emptyset_{corr}(r_{ij-l_0}) \quad (2)$$

Here, l_0 is offset distance and ε_{AA} (=ε_{CC}) is energy constant. Potential (2) and l_0 were introduced to stabilize the rock-salt structure of AC solid phase. l_0 is set to be $l_0 \equiv l_a(\sqrt{2}-1)$, where l_a is the lattice constant of AC rock-salt crystal.

The size of simulation box is set to be $L \times L \times \alpha L$, where αL is the system height (set α=2 in this article). Here the typical system size is set to be $L = 32\ l_a$. Initially, the substrate with four layer-thick solid consisting of A and C particles with rock-salt order is fixed on the bottom wall. Above the substrate, a flat layer of B-particle solvent is placed in the simulation of the VLS process, while no solvent is added to the VS process. The side walls have a periodic boundary condition. The temperature of the system is controlled on the top and bottom walls. The particle bath densities of A particles ρ_A^{sup}, of A' particles $\rho_{A'}^{sup}$, and of C particles ρ_C^{sup} are set independently, and each species is supplied from the top wall. All physical parameters treated in this program are normalized by ε_{AC}, the diameter of A particle σ_A, and the particle mass m. This normalization leads to dimensionless temperature and time parameters of k_{BT}/ε_{AC} and $t\sqrt{\varepsilon_{AC}/m}/\sigma_A$, respectively. In this article, the value of each L- parameter is set as follows: $\sigma_{A'}$=σ_C= σ_A, σ_B=1.44, ε_{AA}=ε_{CC} =0.2, ε_{BB} =0.45, ε_{AB}=0.493 and ε_{CB}=0.258. Temperature is set to be 0.27.

S7. Comparison with previous works on the resistivity of na(2)nowires

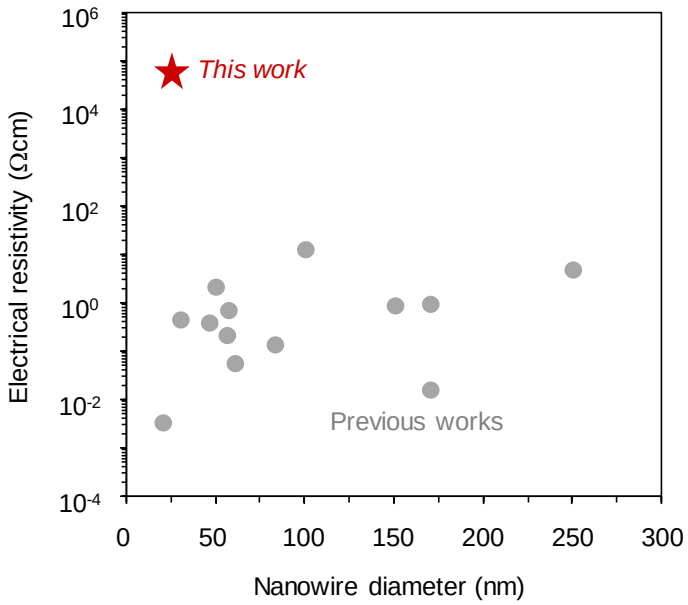

Figure S7 Comparison between the present SnO_2 nanowires and previous works on the electrical resistivity.

Figure S7 shows the comparison between this work and the previous works as to the electrical resistivity of SnO_2 nanowires for various nanowire diameters. Fabricated SnO_2 nanowire in this study showed the almost 3-4 orders of magnitude higher electrical resistivity compared with previous works including *Appl. Phys. Lett.* **107**, 233503 (2015), *Adv. Funct. Mater.* **21,** 474 (2011), *Mater. Today* **14,** 42 (2011), *Solid State Commun.* **130,** 313 (2004), *Appl. Phys. Lett.* **89,** 093114 (2006), *Nano Lett.* **4,** 403 (2004), *ACS Sensor.* **1,** 997 (2016), *Nanotechnology* **17**, 5577 (2006), *J. Mater. Chem.* **22,** 24012 (2012), *Adv. Funct. Mater.* **25,** 3157 (2015), *Appl. Phys. Lett.* **95,** 053105 (2009), *ACS Appl. Mater. Interfaces* **3,** 3097 (2011), *Adv. Mater.* **15,** 1754 (2003), *Biosensors and Bioelectronics* **25,** 2436 (2010), *Sens. Actuators B* **121,** 3 (2007). This is because the unintentional doping effect induced by VS crystal growth could not be avoided. In this study, the unintentional doping was drastically suppressed by strictly controlling the occurrence of VS crystal growth.

S8. Oxygen partial pressure effect on the electrical resistivity of $SnO_{2-\delta}$ thin films deposited on

Temperature: 300ºC

Oxygen pressure 10^{-3}-10Pa (in Ar 10Pa)

On Al_2O_3 (11-20) substrate

Deposition time 30min

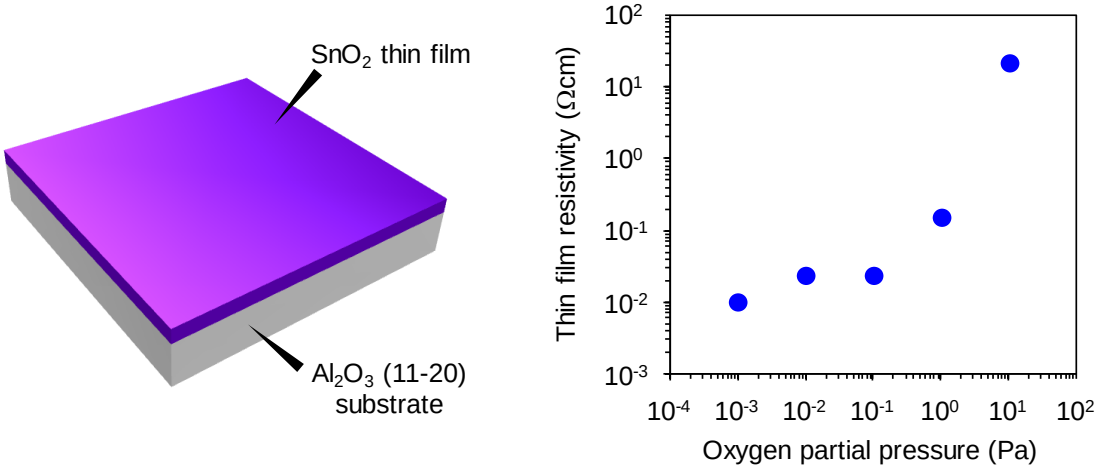

Figure S8 Effect of oxygen partial pressure on the electrical resistivity of $SnO_{2-\delta}$ thin films.

Figure S8 shows the effect of oxygen partial pressure on the electrical resistivity of $SnO_{2-\delta}$ films grown in Al_2O_3 (11-20) substrate. The deposition temperature and time are 300ºC and 30 min, respectively. The oxygen partial pressure is ranged from 10^{-3} to 10 Pa with the constant total pressure 10 Pa of Ar gas. Four-probe measurements were performed to measure the electrical resistivity of fabricated films. As can be seen in the figure, the film resistivity decreased with decreasing the oxygen partial pressure.